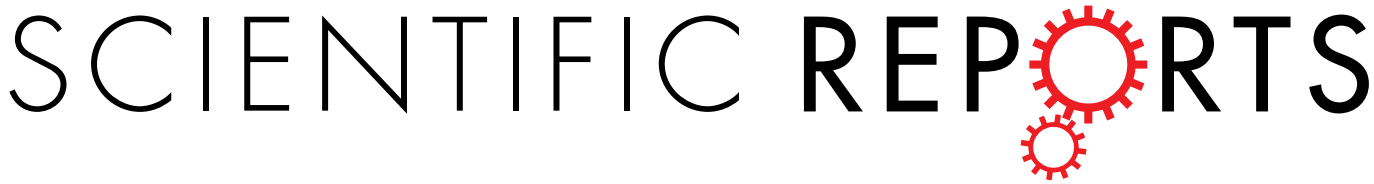

OPEN

Dirac and Weyl Semimetal in *XY*Bi (*X* = Ba, Eu; *Y* = Cu, Ag and Au)

Yongping Du[1], Bo Wan[1], Di Wang[1], Li Sheng[1,2], Chun-Gang Duan[3] & Xiangang Wan[1,2]

Received: 23 April 2015
Accepted: 28 August 2015
Published: 24 September 2015

Weyl and Dirac semimetals recently stimulate intense research activities due to their novel properties. Combining first-principles calculations and effective model analysis, we predict that nonmagnetic compounds Ba*Y*Bi (*Y* = Au, Ag and Cu) are Dirac semimetals. As for the magnetic compound Eu*Y*Bi, although the time reversal symmetry is broken, their long-range magnetic ordering cannot split the Dirac point into pairs of Weyl points. However, we propose that partially substitute Eu ions by Ba ions will realize the Weyl semimetal.

Following the discovery of topological insulator (TI)[1,2], there has been considerable research interest in studying the Weyl semimetal (WSM), the first metallic topologically nontrivial matter[3–6]. In WSM, non-degenerate valence and conduction bands touch at an accidental degeneracy point in a three-dimensional (3D) Brillouin zone, and its low energy physics is approximated by the Weyl equation[3,4]. Weyl points, the nondegenerate linear touchings of the bulk bands, always come in pair, and they are robust due to the protection by the topology of the band structure. The most remarkable feature of WSM is the Fermi arc surface states[3]. Several compounds, including pyrochlore iridates[3], TI based heterostructures[7], $HgCr_2Se_4$[8] and many other systems[9–13] had been theoretically predicted as promising WSMs. The indication about realization of WSM have been reported[14–16]. Very recently, the noncentrosymmetric and nonmagnetic transition-metal monophosphide are predicted as WSM[17,18] and the Fermi arc, as the smoking-gun feature, has been confirmed experimentally[19–23].

Same as the WSM, the Dirac semimetal (DSM) is also a 3D analog of graphene[24–27]. But in contrast with Weyl point, the Dirac point has four-fold degeneracy, and does not possess a topological number, consequently the Dirac point is not robust against the external perturbations and usually hard to be realized. Thus the 3D DSM receive much less attention until the discovery of Na_3Bi[28] and Cd_3As_2[29]. Wang *et al.* find that there is a paired 3D bulk Dirac points exist on the k_z axis of Na_3Bi[28] and Cd_3As_2[29], and these Dirac points are protected by the crystal symmetry thus are stable[28,29]. The theoretical prediction of DSM in Na_3Bi and Cd_3As_2[28,29] had been quickly confirmed by the subsequent photoemission measurement[30–33]. This immmediately triggers a new wave of research to explore the unique properties associated with the 3D Dirac points in the DSM[30–36]. Unfortunately, Na_3Bi is not stable in air while arsenic limits the application of Cd_3As_2. Therefore searching new 3D DSM that is stable in nature and less toxic is of both fundamental and technological importance.

In this paper, based on the density functional theory (DFT) calculations and effective low energy models, we predict that Ba*Y*Bi (*Y* = Au, Ag and Cu) are promising 3D Dirac materials. For BaAuBi, the nontrivial topology is due to the band inversion of the Bi-*p* bonding and antibonding states, while for the BaAgBi and BaCuBi, the band inversion happens between the Ag/Cu *s* and Bi *p* orbital. Protected by the C_3 rotation symmetry, the Dirac points locate along the $\Gamma - A$ line. The magnetic configuration in Eu*Y*Bi indeed break the time reversal symmetry, however cannot split the Dirac point into two Weyl points. We propose that partially substituting Eu by Ba, i.e. alloy compound $Eu_xBa_{(1-x)}Ag(Au)Bi$, which could be grown using molecular beam epitaxy (MBE) technique, is a promising way to realize the WSM.

[1]National Laboratory of Solid State Microstructures and Department of Physics, Nanjing University, Nanjing 210093, China. [2]Collaborative Innovation Center of Advanced Microstructures, Nanjing University, Nanjing 210093, China. [3]Key Laboratory of Polar Materials and Devices, Ministry of Education, East China Normal University, Shanghai 200062, China. Correspondence and requests for materials should be addressed to X.W. (email: xgwan@nju.edu.cn)

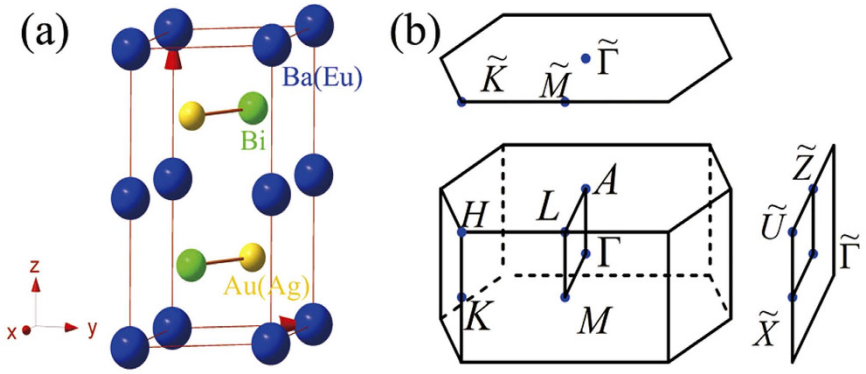

Figure 1. (**a**) Crystal structure of BaAuBi. BaAgBi and BaCuBi have similar structure. (**b**) Brillouin zone of bulk and the projected surface Brillouin zones of (001) and (010) planes.

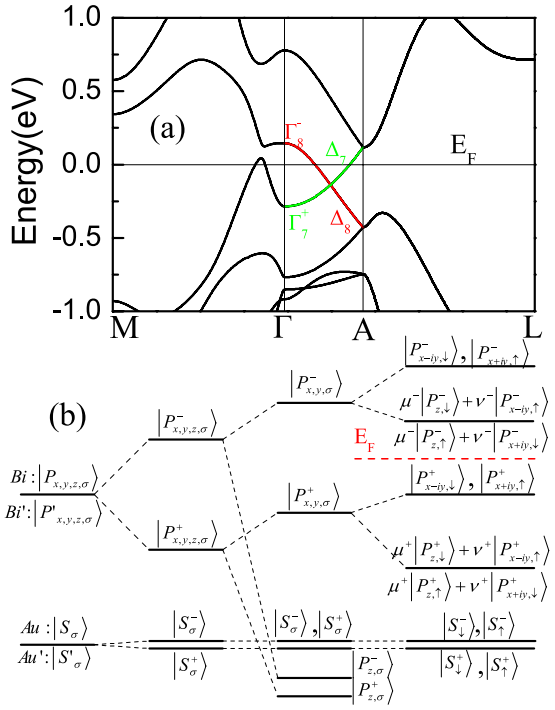

Figure 2. (**a**) Electronic structure of BaAuBi. Green and red line highlights the different irreducible representation along $\Gamma - A$ line. (**b**) Band evolution near Fermi energy of BaAuBi at Γ point, red dashed line stands for the Fermi energy (see main text for detailed description).

Results and Discussion

BaYBi (Y = Au, Ag, Cu) crystallize in the same hexagonal ZrBeSi type structure with space group $P6_3/mmc$ (D_{6h}^4)[37]. The crystal structure of BaAuBi is shown as an example in Fig. 1, in which Au and Bi ions form honeycomb lattice layers stacking along c axis and sandwiched by trigonal layers formed by Ba atoms. There are two formula units in the primitive unit cell, and the six atoms in the unit cell locate at three nonequivalent crystallographic sites: Ba atoms occupy the $2a\left(0, 0, \frac{1}{2}\right)$, while Au and Bi reside on the $2c\left(\frac{1}{3}, \frac{2}{3}, \frac{1}{4}\right)$ and $2d\left(\frac{2}{3}, \frac{1}{3}, \frac{1}{4}\right)$ sites respectively[37]. There is no free internal coordinates, and the lattice constants are the only structural parameter for BaYBi lattice. We optimize the lattice parameter and for all of the three compounds, our numerical lattice constants are in good agreements with experiments, and the small discrepancy between the numerical and experimental structure has negligible effect on the electronic structure. Hence, the following results are obtained based on the experimental structure, unless stated specifically.

We first calculate the electronic structure of BaAuBi, and show the results in Fig. 2(a). The Ba in BaAuBi is highly ionic, has negligible contribution to the states around Fermi level. Au-6s and 5d bands

mainly located at −4 to −1 eV, and −6 to −4 eV, respectively. The Bi-6*s* is basically located about −11 eV below the Fermi level. The valence and conduction bands are dominated by the Bi-6*p* bonding and antibonding states. Checking the wave function, we find that at the Γ point the Bi-6*p* antibonding state is higher than the Bi-6*p* bonding state, however at the *A* point, the odd-parity state is about 0.545 eV lower in energy than even-parity state.

In order to understand the mechanism of the band inversion, we illustrate the band evolution at the Γ point of BaAuBi in Fig. 2(b). As discussed above, the states near Fermi level are primarily contributed by the Bi-6*p* orbital, with also the Au-6*s* state. Since the two Bi atoms (Bi and Bi′) in the unit cell are related to each other by the inversion symmetry, similar with ref. 38,39, we combine the Bi-6*p* orbitals to form the hybridized states and label the bonding and antibonding states as $|P^+_{x,y,z}\rangle (=\frac{1}{\sqrt{2}}(|\mathrm{Bi}, p_{x,y,z}\rangle - |Bi', p_{x,y,z}\rangle))$ and $|P^-_{x,y,z}\rangle (=\frac{1}{\sqrt{2}}(|\mathrm{Bi}, p_{x,y,z}\rangle + |Bi', p_{x,y,z}\rangle))$ respectively, where the superscripts +/− denote the parity of the corresponding states. According to the point group symmetry, the p_z orbital split from the p_x and p_y orbitals while the latter two are still degenerate as shown in the Fig. 2(b). Finally, we consider the effect of SOC. The $|P^+_{x+iy,\uparrow}\rangle$ and $|P^+_{x-iy,\downarrow}\rangle$ states are pushed up by the SOC, while the $|P^-_{z,\uparrow}\rangle (|P^-_{z,\downarrow}\rangle)$ will mix with $|P^-_{x+iy,\downarrow}\rangle (|P^-_{x-iy,\uparrow}\rangle)$, consequently the bonding ($|P^+_{x+iy,\uparrow}\rangle$ and $|P^+_{x-iy,\downarrow}\rangle$) and antibonding states ($\mu^-|P^-_{z,\uparrow}\rangle + \upsilon^-|P^-_{x+iy,\downarrow}\rangle$ and $\mu^-|P^-_{z,\downarrow}\rangle + \upsilon^-|P^-_{x-iy,\uparrow}\rangle$) are close to each other at the Γ point, and the band inversion occurs at the *A* point as shown in Fig. 2.

Along $\Gamma - A$ line the C_3 symmetry is preserved, by the symmetry analysis the two relevant bands along this line belong to different representations (Δ_7 and Δ_8 as shown in Fig. 2(a). See Additional Data for the detail). Thus the hybridization between these bands is strictly forbidden, which results in the protected band crossing as shown in Fig. 2(a). The linear band dispersions associated with Dirac points near the Fermi surface will contribute a high-field unsaturated linear magnetoresistance[40,41], we thus believe such novel properties may also be observed in BaAuBi, although the Dirac point is located slightly below the Fermi level as shown in Fig. 2(a).

Since the topological nature is determined by the Δ_7 and Δ_8 bands, based on the projection-operator method (see Additional Data), we build the effective Hamiltonian by using the four relevant states as basis vectors (in the order of $|P^+_{x+iy,\uparrow}\rangle$, $\mu^-|P^-_{z,\downarrow}\rangle + \upsilon^-|P^-_{x-iy,\uparrow}\rangle$, $|P^+_{x-iy,\downarrow}\rangle$, $\mu^-|P^-_{z,\uparrow}\rangle + \upsilon^-|P^-_{x+iy,\downarrow}\rangle$) at Γ point. We neglect all of other states, since they are far from the Fermi level and do not involve into the band inversion, and the Hamiltonian can be written as:

$$H_{eff} = \varepsilon_0(\mathbf{k}) + \begin{pmatrix} M(\mathbf{k}) & A(\mathbf{k})k_+ & 0 & Bk_z k_+^2 \\ A(\mathbf{k})k_- & -M(\mathbf{k}) & -Bk_z k_+^2 & 0 \\ 0 & -Bk_z k_-^2 & M(\mathbf{k}) & A(\mathbf{k})k_- \\ Bk_z k_-^2 & 0 & A(\mathbf{k})k_+ & -M(\mathbf{k}) \end{pmatrix} \quad (1)$$

where $\varepsilon_0(\mathbf{k}) = C_0 + C_1 k_z^2 + C_2\left(k_x^2 + k_y^2\right)$, $M(\mathbf{k}) = M_0 - M_1 k_z^2 - M_2\left(k_x^2 + k_y^2\right)$, $A(\mathbf{k}) = A_0 + A_1 k_z^2 + A_2\left(k_x^2 + k_y^2\right)$ and $k_\pm = k_x \pm ik_y$. The parameters in the above formula are material dependent, and by fitting the DFT calculated band dispersion, we obtain $C_0 = -0.06978\,eV$, $C_1 = -0.34038\,eV\cdot Å^2$, $C_2 = 2.25\,eV\cdot Å^2$, $M_0 = -0.21537\,eV$, $M_1 = -1.9523\,eV\cdot Å^2$, $M_2 = -7.9507\,eV\cdot Å^2$, and $A_0 = 1.3668\,eV\cdot Å$. Solving the above eigenvalue problem, we obtain $E(\mathbf{k}) = \varepsilon_0(\mathbf{k}) \pm \sqrt{M(\mathbf{k})^2 + A(\mathbf{k})^2 k_+ k_- + |B|^2 k_z^2 k_+^2 k_-^2}$, and at $\mathbf{k}_c = \left(0,0, \pm\sqrt{\frac{M_0}{M_1}}\right)$, we get the gapless solutions. In the vicinity of $\mathbf{k}_c$ and neglect the high-order terms, $E(\mathbf{k'})$ would be equal to $\varepsilon_0(\mathbf{k'}) \pm \sqrt{4M_1^2\mathbf{k}_c^2\delta k_z^2 + A^2(\mathbf{k}_c)\left(\delta k_x^2 + \delta k_y^2\right)}$ ($\delta k_{x,y,z}$ are small displacement from $\mathbf{k}_c$), which is a linear dispersion and suggests in neighbourhood of $\mathbf{k}_c$, our effective Hamiltonian is nothing but 3D anisotropic massless Dirac fermions. A 3D Dirac semimetal state can also be realized at the critical point of the topological phase transition between a band insulator and a 3D topological insulator[42,43]. Different from this case, the Dirac points in BaAuBi are protected by the C_3 rotation symmetry, thus very robust.

We also investigate the BaAgBi and BaCuBi. The electronic properties of BaCuBi are very similar with that of BaAgBi, we thus only report results of BaAgBi. As shown in Fig. 3(b), significantly different with the Au-6*s* state in BaAuBi, the Ag-5*s* orbit in BaAgBi is higher in energy than Bi-6*p* state, consequently the states closed to the Fermi level become $|P^-_{x+iy,\uparrow}\rangle$, $|P^-_{x-iy,\downarrow}\rangle$ and $|S^+_\uparrow\rangle$, $|S^+_\downarrow\rangle$. Similar with the case in Na_3Bi[28], due to the strong SOC of Bi-6*p*, the $|P^-_{x+iy,\uparrow}\rangle$ and $|P^-_{x-iy,\downarrow}\rangle$ states will be pushed up, which result in the band inversion at Γ point. This inversion is confirmed by our DFT calculation, as shown in Fig. 3(a), at the Γ point, the $|P^-_{x+iy,\uparrow}\rangle$, $|P^-_{x-iy,\downarrow}\rangle$ is higher than $|S^+_\uparrow\rangle$, $|S^+_\downarrow\rangle$ by about 0.34 eV. Along $\Gamma - A$ line, these two bands belongs to different representations (Δ_7 and Δ_8), thus there is also a unavoidable crossing point located at $\Gamma - A$ line. It is also easy to prove that the band dispersion is linear around the band touching points. Thus, the crossing points are the Dirac points.

The Dirac points in BaAgBi are doubly degenerate due to inversion and time-reversal symmetries, and upon breaking the time reversal symmetry[3] or inversion symmetry[42,43] a Dirac cone will split into two Weyl nodes separated in momentum space. This family of intermetallic compound with

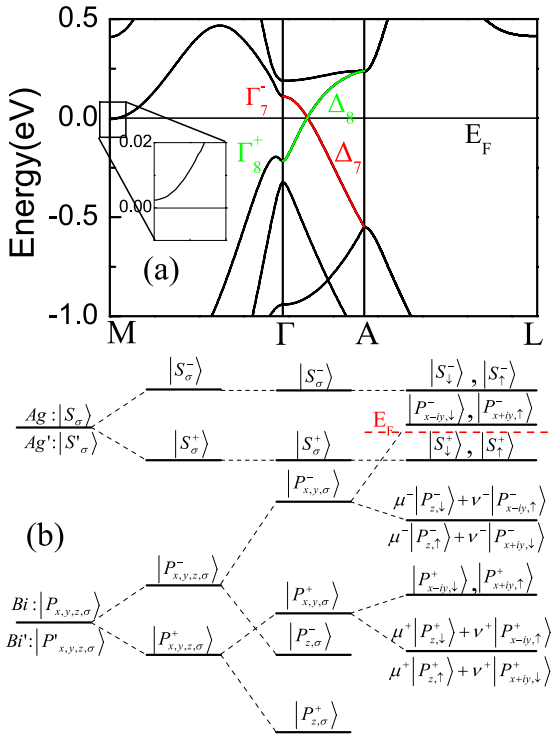

Figure 3. (**a**) Electronic structure of BaAgBi, Green and red line highlights the different irreducible representation along $\Gamma - A$ line. (**b**) Band evolution around Fermi energy of BaAgBi at Γ point, red dashed line stands for the Fermi energy.

hexagonal structure indeed has several members with magnetic ion Eu: Eu*XY* ($X =$ Cu, Au, Ag; $Y =$ As, Sb, Bi)[37,44,45]. Experiments confirm that some of them indeed possess long-range magnetic configuration[44]. Unfortunately, the Eu^{2+} spins align ferromagnetically with the *ab* plane, but antiferromagnetically along the *c*-axis[45], therefore the exchange field is exactly cancelled at the *XY*-plane of Eu*XY*. Thus breaking the time reversal symmetry by this type of antiferromagnetic configuration cannot split the Dirac points, and the compounds of Eu*XY* have no chance to become WSM.

We, however, expect that substituting part of Eu ions by Ba ions, the two antiferromagnetically coupled Eu plane in $Eu_xBa_{1-x}AgBi$ may not exactly cancel each other, and then there is a chance the compound becomes WSM. To confirm this expectation, we then performed another calculation on $Eu_{0.5}Ba_{0.5}AgBi$, in which we replace one of the two antiferromagnetically coupled Eu plane in the unit cell by Ba. According to our calculation, the *c* axis is the magnetic easy axis, this magnetization does not break the C_3 rotation symmetry, consequently as shown in Fig. 4(a), the Dirac point indeed splits into two Weyl points as marked by red circle. There is also two other Weyl points slightly above/below the Weyl nodes marked by red circle. The Weyl nodes are very close to the Fermi energy as shown in Fig. 4(a), thus, the phenomena associated with the chiral anomaly[46–48] also exist in $Eu_{0.5}Ba_{0.5}AgBi$. Fig. 4(b) shows the Fermi arcs which connect projected bulk Weyl points of opposite chirality. Thus we believe to grow it by the cutting edge film growth technique like MBE and to explore the possible WSM are a very interesting topic.

In summary, based on density-functional calculation and effective model analysis, we propose that the Ba*Y*Bi ($Y =$ Au, Ag and Cu) are 3D Dirac semimetals. The nontrivial topological feature is due to *p-p* inversion for BaAuBi and *s-p* band inversion for BaAgBi and BaCuBi, and their Dirac points are protected by the C_3 rotation symmetry and thus are very robust. Their magnetic cousins, i.e Eu*Y*Bi ($Y =$ Au, Ag and Cu) are not Weyl semimetals. However, partial substitution of Eu with Ba ions in Eu*Y*Bi could result in the Weyl semimetal. Furthermore, our numerical calculation also confirm that a uniaxial strain along *a*-axis, which breaks the C_3 rotation symmetry, will drive BaAgBi into topological insulator.

Note. When finalizing our work, we became aware of a recent study by Borisenko *et al.*[49], in which the authors also predict BaAgBi is a possible 3D DSM, agreeing with our conclusion.

Methods

The electronic band structure calculations have been carried out using the full potential linearized augmented plane wave method as implemented in WIEN2K package[50]. The modified Becke-Johnson exchange potential together with local-density approximation for the correlation potential (MBJLDA) has been used here to obtain accurate band inversion strength and band order[51]. A $16 \times 16 \times 7$ mesh

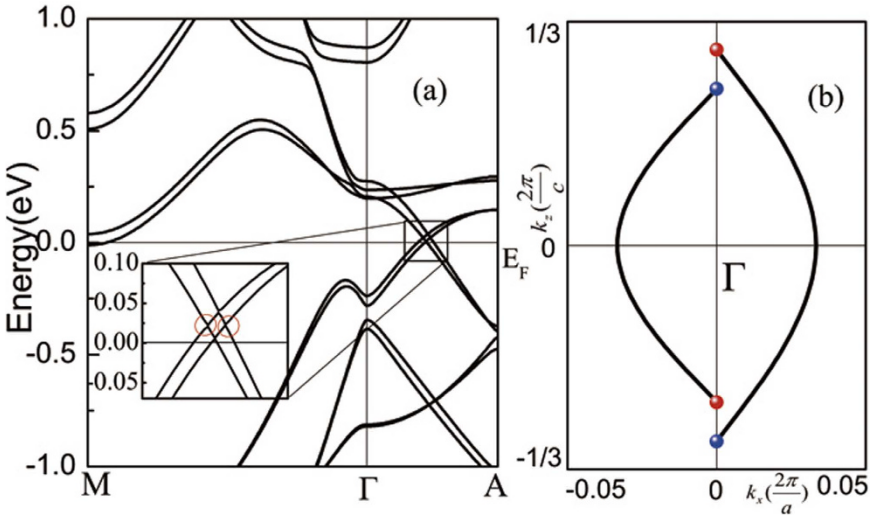

Figure 4. Band structure and surface state of $Eu_{0.5}Ba_{0.5}AgBi$. (a) Calculated band structure of $Eu_{0.5}Ba_{0.5}AgBi$. (**b**)The sketch of the Fermi arcs connecting projected bulk Weyl points of opposite chirality. The blue and red dots denote the Weyl points with opposite chirality.

is used for the Brillouin zone integral. Using the second-order variational procedure, we include the spin-orbital coupling (SOC) interaction.

The tight-binding model has been established by using Slater-Koster method[52]. 5s orbit of Ag atom and three 6p orbits of Bi atom are taken as basis. The tight-binding model has been used to simulate the bulk band structure with Weyl points as found by our LSDA + SO + U calculation. To calculate the surface state and Fermi arc, we build the (010) slab of a thickness of 85 unit-cells.

Additional Data

Effective Hamiltonian for BaAuBi. The conduction and valence bands of BaAuBi are mainly contributed by four states: $|P^+_{x+iy,\uparrow}\rangle$, $\mu^-|P^-_{z,\downarrow}\rangle + \upsilon^-|P^-_{x-iy,\uparrow}\rangle$, $|P^+_{x-iy,\downarrow}\rangle$ and $\mu^-|P^-_{z,\uparrow}\rangle + \upsilon^-|P^-_{x+iy,\downarrow}\rangle$, we thus use

Γ matrices	representation	T
Γ_0, Γ_5	R_1	+
$\{\Gamma_1, \Gamma_2\}$	R_{14}	+
$\{\Gamma_3, \Gamma_4\}$	R_{15}	+
Γ_{12}, Γ_{34}	R_2	−
$\Gamma_{14}+\Gamma_{23}$	R_3	−
$\Gamma_{13}-\Gamma_{24}$	R_4	−
$\{\Gamma_{13}+\Gamma_{24}, \Gamma_{14}-\Gamma_{23}\}$	R_6	−
$\{\Gamma_{15}, \Gamma_{25}\}$	R_{14}	−
$\{\Gamma_{35}, \Gamma_{45}\}$	R_{15}	−
***d*(*k*)**	**representation**	**T**
$C, k_z^2, k_x^2 + k_y^2$	R_1	+
$\left\{k_x k_y k_z, \frac{1}{2}\left(k_x^2 - k_y^2\right)k_z\right\}$	R_{14}	−
$\left\{k_x, k_y\right\}, \left\{\left(k_x^2 + k_y^2\right)k_x, \left(k_x^2 + k_y^2\right)k_y\right\}, \left\{k_z^2 k_x, k_z^2 k_y\right\}$	R_{15}	−
$k_z, \left(k_x^2 + k_y^2\right)k_z, k_z^3$	R_{11}	−
$\left\{k_x^2 - k_y^2, k_x k_y\right\}$	R_5	+
$\{k_x k_z, k_y k_z\}$	R_6	+
$k_x^3 - 3k_x k_y^2$	R_{12}	−
$k_y^3 - 3k_x^2 k_y$	R_{13}	−

Table 1. The character table of Dirac Γ matrices and the polynomials of the momentum *k* for BaAuBi.

Γ matrices	representation	T
Γ_0, Γ_5	R_1	+
$\{\Gamma_1, \Gamma_2\}$	R_{14}	−
$\{\Gamma_3, \Gamma_4\}$	R_{15}	−
Γ_{12}, Γ_{34}	R_2	−
$\Gamma_{14}-\Gamma_{23}$	R_3	−
$\Gamma_{13}+\Gamma_{24}$	R_4	−
$\{\Gamma_{13}-\Gamma_{24}, \Gamma_{14}+\Gamma_{23}\}$	R_6	−
$\{\Gamma_{15}, \Gamma_{25}\}$	R_{14}	+
$\{\Gamma_{35}, \Gamma_{45}\}$	R_{15}	+
$\boldsymbol{d(k)}$	**representation**	**T**
$C, k_z^2, k_x^2+k_y^2$	R_1	+
$\left\{k_xk_yk_z, \frac{1}{2}\left(k_x^2-k_y^2\right)k_z\right\}$	R_{14}	−
$\left\{k_x, k_y\right\}, \left\{\left(k_x^2+k_y^2\right)k_x, \left(k_x^2+k_y^2\right)k_y\right\}, \left\{k_z^2k_x, k_z^2k_y\right\}$	R_{15}	−
$k_z, \left(k_x^2+k_y^2\right)k_z, k_z^3$	R_{11}	−
$\left\{k_x^2-k_y^2, k_xk_y\right\}$	R_5	+
$\{k_xk_z, k_yk_z\}$	R_6	+
$k_x^3-3k_xk_y^2$	R_{12}	−
$k_y^3-3k_x^2k_y$	R_{13}	−

Table 2. The character table of Dirac matrices and the function $d(k)$ of BaAgBi.

D_{6h}^4	Γ_7^+	Γ_8^+	Γ_9^+	Γ_7^-	Γ_8^-	Γ_9^-
C_{6v}^1	Δ_7	Δ_8	Δ_9	Δ_7	Δ_8	Δ_9

Table 3. The compatibility relations between the double group of C_{6v}^1 and D_{6h}^4.

these states as the basis to build the effective model Hamiltonian at the Γ point of BZ. As a 4×4 hermitian matrix, the effective Hamiltonian can be written as $H=\varepsilon(\mathbf{k})\mathbf{I}+\sum_i d_i(\mathbf{k})\Gamma_i+\sum_{ij} d_{ij}(\mathbf{k})\Gamma_{ij}$, where $\mathbf{I}$ is the 4×4 identity matrix, Γ_i and Γ_{ij} are Dirac matrices, $\varepsilon(\mathbf{k})$, $d_i(\mathbf{k})$, and $d_{ij}(\mathbf{k})$ are function of momentum k.

The Hamiltonian should be invariant under the operation of crystal symmtery and time reversal symmtery. This requires the function $d_i(\mathbf{k})$ $[d_{ij}(\mathbf{k})]$ and the associated Γ_i $[\Gamma_{ij}]$ matrices belong to the same irreducible representation. Thus the key problem is to determine the irreducible representation for $d_i(\mathbf{k})$ $[d_{ij}(\mathbf{k})]$ and Γ matrices, which can be done by the projection-operator method.

The Dirac Γ matrices can be written as $\Gamma_1=\sigma_1\otimes\tau_1$, $\Gamma_2=\sigma_2\otimes\tau_1$, $\Gamma_3=\sigma_3\otimes\tau_1$, $\Gamma_4=\sigma_0\otimes\tau_2$, $\Gamma_5=\sigma_0\otimes\tau_3$, and $\Gamma_{ab}=[\Gamma_a, \Gamma_b]/2i$[39]. The projection operator is defined as $p^i=\frac{l_i}{g}\sum_{R\in G}\chi^i(R)P_R$, where g is the group order, l_i is the dimension of the ith representation, R denotes the group element i.e. the symmetry operation, $\chi^i(R)$ represent the character of group element R in ith representation, P_R is the operator of group element R.

The double group of D_{6h}^4 has 18 classes, and their irreducible representations are denoted as R_1 to R_{18}[53], and its character table can be found in ref. 45. Based on the basis mentioned above, one can easily work out the transformation matrix D_R for symmetry operator P_R, which allow us to apply the projection operator p^i on Γ_a: $p^i\Gamma_a=\frac{l_i}{g}\sum_{R\in G}\chi^i(R)D_R\Gamma_aD_R^{-1}$, consequently determine the irreducible representation of Γ_a. Using the same process, one can also determine the irreducible representation for the polynomials of $\mathbf{k}$ up to $O(\mathbf{k}^3)$. We present the irreducible representation of Dirac Γ matrices and polynomials of $\mathbf{k}$, and their transformation under time reversal in Table 1.

With the Table 1, the effective model Hamiltonian of BaAuBi can be easily expressed as: $H=\varepsilon_0(\mathbf{k})+M(\mathbf{k})\Gamma_5+A(\mathbf{k})(k_x\Gamma_{45}+k_y\Gamma_{35})+Bk_z((k_x^2-k_y^2)\Gamma_{25}+2k_xk_y\Gamma_{15})$, where $\varepsilon_0(\mathbf{k})=C_0+C_1k_z^2+C_2(k_x^2+k_y^2)$, $M(\mathbf{k})=M_0-M_1k_z^2-M_2(k_x^2+k_y^2)$, $A(\mathbf{k})=A_0+A_1k_z^2+A_2(k_x^2+k_y^2)$.

Effective Hamiltonian for BaAgBi. For BaAgBi, the conduction bands are Ag-5*s* states, while the valence bands are Bi-6*p* states, thus the four basis become $|S_\uparrow^+\rangle$, $|P_{x+iy,\uparrow}^-\rangle$, $|S_\downarrow^+\rangle$ and $|P_{x-iy,\downarrow}^-\rangle$. We list the character table of Γ matrices and the function $d(\mathbf{k})$ (expanded as polynomials of the momentum k)

and their transformation under time reversal in Table 2. Based on Table 2, one can get the effective model Hamiltonian for BaAgBi:
$H = \varepsilon_0(\mathbf{k}) + M(\mathbf{k})\Gamma_5 + A(\mathbf{k})(k_x\Gamma_3 - k_y\Gamma_4) + Bk_z((k_x^2 - k_y^2)\Gamma_1 + 2k_xk_y\Gamma_2)$, where $\varepsilon_0(\mathbf{k}) = C_0 + C_1k_z^2 + C_2(k_x^2 + k_y^2)$, $M(\mathbf{k}) = M_0 - M_1k_z^2 - M_2(k_x^2 + k_y^2)$, $A(\mathbf{k}) = A_0 + A_1k_z^2 + A_2(k_x^2 + k_y^2)$.

Band representation. At the Γ point of BZ, each state should belong to an irreducible representation of the double group of D_{6h}^4. Again, applying the projection operator onto the conduction and valence states of BaAuBi, we find that $|P_{x+iy,\uparrow}^+\rangle$ and $|P_{x-iy,\downarrow}^+\rangle$ belong to representation Γ_7^+, while $\mu^-|P_{z,\downarrow}^-\rangle + \upsilon^-|P_{x-iy,\uparrow}^-\rangle$ and $\mu^-|P_{z,\uparrow}^-\rangle + \upsilon^-|P_{x+iy,\downarrow}^-\rangle$ belong to representation Γ_8^-, which had been marked in Fig. 2(a). Different from Γ point, the symmetry of $\Gamma - A$ line is C_{6v}^1. We show the compatibility relations between the double group of D_{6h}^4 and C_{6v}^1 in Table 3. It is clear that the representation Γ_7^+ and Γ_8^-, evolute to Δ_7 and Δ_8, respectively.

For BaAgBi, the valence/conduction states at the Γ point of BZ belong Γ_8^+/Γ_7^-, and will change to Δ_8 and Δ_7 along $\Gamma - A$ line according to Table 3.

References

1. Hasan, M. Z. & Kane, C. L. Colloquium: Topological insulators. *Rev. Mod. Phys.* **82,** 3045 (2010).
2. Qi, X. L. & Zhang, S.-C. Topological insulators and superconductors. *Rev. Mod. Phys.* **83,** 1057 (2011).
3. Wan, X., Turner, A. M., Vishwanath, A. & Savrasov, S. Y. Topological semimetal and Fermi-arc surface states in the electronic structure of pyrochlore iridates. *Phys. Rev. B* **83,** 205101 (2011).
4. Balents, L. Weyl electrons kiss. *Physics* **4,** 36 (2011).
5. Ando, Y. Topological Insulator Materials. *J. Phys. Soc. of Jpn*. **82,** 102001 (2013).
6. Yang, K.-Y., Lu, Y.-M. & Ran, Y. Quantum Hall effects in a Weyl semimetal: Possible application in pyrochlore iridates. *Phys. Rev. B* **84,** 075129 (2011).
7. Burkov, A. A. & Balents, L. Weyl Semimetal in a Topological Insulator Multilayer. *Phys. Rev. Lett*. **107,** 127205 (2011).
8. Xu, G., Weng, H. M., Wang, Z., Dai, X. & Fang, Z. Chern Semimetal and the Quantized Anomalous Hall Effect in $HgCr_2Se_4$. *Phys. Rev. Lett*. **107,** 186806 (2011).
9. Bulmash, D., Liu, C.-X. & Qi, X.-L. Prediction of a Weyl semimetal in $Hg_{1-x-y}Cd_xMn_yTe$. *Phys. Rev. B* **89,** 081106 (2014).
10. Halász, G. & Balents, L. Time-reversal invariant realization of the Weyl semimetal phase. *Phys. Rev. B* **85,** 035103 (2012).
11. Liu, J. & Vanderbilt, D. Weyl semimetals from noncentrosymmetric topological insulators. *Phys. Rev. B* **90,** 155316 (2014).
12. Wan, X., Vishwanath, A. & Savrasov, S. Y. Computational Design of Axion Insulators Based on 5d Spinel Compounds. *Phys. Rev. Lett.* **108,** 146601 (2012).
13. Mañes, J. L. Existence of bulk chiral fermions and crystal symmetry. *Phys. Rev. B* **85,** 155118 (2012).
14. Ueda, K. *et al.* Variation of Charge Dynamics in the Course of Metal-Insulator Transition for Pyrochlore-Type $Nd_2Ir_2O_7$ *Phys. Rev. Lett*. **109,** 136402 (2012).
15. Chu, J.-H. *et al.* Linear magnetoresistance and time reversal symmetry breaking of pyrochlore iridates $Bi_2Ir_2O_7$. arXiv:1309.4750 (2013).
16. Kim, H.-J. *et al.* Dirac versus Weyl Fermions in Topological Insulators: Adler-Bell-Jackiw Anomaly in Transport Phenomena. *Phys. Rev. Lett*. **111,** 246603 (2013).
17. Weng, H. M., Fang, C., Fang, Z., Bernevig, B. A. & Dai, X. Weyl Semimetal Phase in Noncentrosymmetric Transition-Metal Monophosphides. *Phys. Rev. X*. **5,** 011029 (2015).
18. Huang, S. M. *et al.* A Weyl Fermion semimetal with surface Fermi arcs in the transition metal monopnictide TaAs class. *Nature Comm*. **6,** 7373 (2015).
19. Xu, S. Y. *et al.* Discovery of Weyl semimetal NbAs. *arXiv:* 1504.01350
20. Xu, S. Y. *et al.* Discovery of a Weyl Fermion semimetal and topological Fermi arcs. *Science* doi: 10.1126/science.aaa9297 (2015).
21. Lv, B. Q. *et al.* Observation of Weyl nodes in TaAs. *arXiv:* 1503.09188
22. Xu, N. *et al.* Observation of Weyl nodes and Fermi arcs in TaP. *arXiv:* 1507.03983
23. Lv, B. Q. *et al.* Experimental Discovery of Weyl Semimetal TaAs. *Phys. Rev. X*. **5,** 031013 (2015).
24. Young, S. *et al.* Dirac Semimetal in Three Dimensions. *Phys. Rev. Lett*. **108,** 140405 (2012).
25. Singh, B. *et al.* Topological electronic structure andWeyl semimetal in the $TlBiSe_2$ class of semiconductors. *Phys. Rev. B* **86,** 115208 (2012).
26. Steinberg, J. A. *et al.* Bulk Dirac Points in Distorted Spinels. *Phys. Rev. Lett*. **112,** 036403 (2014).
27. Yang, B. J. & Nagaosa, N. Classification of stable three-dimensional Dirac semimetals with nontrivial topology. *Nature Comm*. **5,** 4898 (2014).
28. Wang, Z. *et al.* Dirac semimetal and topological phase transitions in A_3Bi (A = Na, K, Rb). *Phys. Rev. B* **85,** 195320 (2012).
29. Wang, Z., Weng, H. M., Wu, Q., Dai, X. & Fang, Z. Three-dimensional Dirac semimetal and quantum transport in Cd_3As_2. *Phys. Rev. B* **88,** 125427 (2013).
30. Liu, Z. K. *et al.* Discovery of a Three-Dimensional Topological Dirac Semimetal, Na_3Bi. *Science* **343,** 864 (2014).
31. Xu, S.-Y. *et al.* Observation of a bulk 3D Dirac multiplet, Lifshitz transition, and nestled spin states in Na_3Bi. arXiv:1312.7624 (2013).
32. Borisenko, S. *et al.* Experimental Realization of a Three-Dimensional Dirac Semimetal. *Phys. Rev. Lett*. **113,** 027603 (2014).
33. Neupane, M. *et al.* Observation of a three-dimensional topological Dirac semimetal phase in high-mobility Cd_3As_2. *Nature Comm*. **5,** 3786 (2014).
34. He, L. P. *et al.* Quantum Transport Evidence for the Three-Dimensional Dirac Semimetal Phase in Cd_3As_2. *Phys. Rev. Lett*. **113,** 246402 (2014).
35. Liang, T. *et al.* Ultrahigh mobility and giant magnetoresistance in the Dirac semimetal Cd_3As_2. *Nature Materials* **14** 280 (2015).
36. Novak, M., Sasaki, S., Segawa, K. & Ando, Y. Large linear magnetoresistance in the Dirac semimetal TlBiSSe. arXiv:1408.2183 (2014).
37. Merlo, F., Pani, M. & Fornasini, M. L. RMX compounds formed by alkaline earths, europium and ytterbium –I. Ternary phases with M = Cu, Ag, Au, X = Sb, Bi. *J. Less-Common Metals* **166,** 319 (1990).
38. Zhang, H. *et al.* Topological insulators in Bi_2Se_3, Bi_2Te_3 and Sb_2Te_3 with a single Dirac cone on the surface. *Nature Phys*. **5,** 438 (2009).
39. Liu, C.-X. *et al.* Model Hamiltonian for topological insulators. *Phys. Rev. B* **82,** 045122 (2010).

40. Wang, K., Graf, D. & Petrovic, C. Quasi-two-dimensional Dirac fermions and quantum magnetoresistance in $LaAgBi_2$. *Phys. Rev. B* **87,** 235101 (2013).
41. May, A. F., McGuire, M. A. & Sales, B. C. Effect of Eu magnetism on the electronic properties of the candidate Dirac material $EuMnBi_2$ *Phys. Rev. B* **90,** 075109 (2014).
42. Murakami, S. Phase transition between the quantum spin Hall and insulator phases in 3D: emergence of a topological gapless phase. *New J. Phys.* **9,** 356 (2007).
43. Murakami, S. & Kuga, S.-I. Universal phase diagrams for the quantum spin Hall systems. *Phys. Rev. B* **78,** 165313 (2008).
44. Michels, G. *et al.* Final-state effects in divalent Eu pnictides. *J. Phys.: Condens. Matter* **6,** 1769 (1994).
45. Tong, J. *et al.* Magnetic properties of EuCuAs single crystal. *J. Alloys Compounds* **602,** 26 (2014).
46. Burkov, A. A. Anomalous Hall Effect in Weyl Metals. *Phys. Rev. Lett.* **113,** 187202 (2014).
47. Burkov, A. A. Chiral Anomaly and Diffusive Magnetotransport in Weyl Metals. *Phys. Rev. Lett.* **113,** 247203 (2014).
48. Son, D. T. & Spivak, B. Z. Chiral anomaly and classical negative magnetoresistance of Weyl metals. *Phys. Rev. B* **88,** 104412 (2013).
49. Gibson, Q. D. *et al.* 3D Dirac semimetals: current materials, design principles and predictions of new materials. arXiv:1411.0005 (2014).
50. Blaha, P., Schwarz, K., Madsen, G. K. H., Kvasnicka, D. & Luitz, J. WIEN2K, An Augmented Plane Wave+ Local Orbitals Program for Calculating Crystal Properties (Karlheinz Schwarz, Technische Universitat Wien, Austria, 2001).
51. Tran, F. & Blaha, P. Accurate Band Gaps of Semiconductors and Insulators with a Semilocal Exchange-Correlation Potential. *Phys. Rev. Lett.* **102,** 226401 (2009).
52. Slater, J. C. & Koster G. F. Simplified LCAO Method for the Periodic Potential Problem. *Phys. Rev.* **94,** 1498 (1954).
53. Bradley, C. J. & Cracknell, A. P. The Mathematical Theory of Symmetry in Solids: Representation Theory for Point Groups and Space Groups, Oxford University Press, reprinted (2011).

Acknowledgements

The work was supported by the National Key Project for Basic Research of China (Grants No. 2011CB922101, 2014CB921104), NSFC under Grants No. 91122035, 11174124, 11374137 and 61125403. The project is also funded by Priority Academic Program Development of Jiangsu Higher Education Institutions. Supported by the program B for Outstanding PhD candidate of Nanjing University.

Author Contributions

X.W. notices the Dirac point in these systems. Y.D. and B.W. perform the first principle calculation. Y.D. and D.W. did the symmetry analysis and the model. X.W. interpret the numerical results and write the paper. All authors contribute to editing the manuscript.

Additional Information

Competing financial interests: The authors declare no competing financial interests.

How to cite this article: Du, Y. *et al.* Dirac and Weyl Semimetal in *XY*Bi (*X*=Ba, Eu; *Y*=Cu, Ag and Au). *Sci. Rep.* **5**, 14423; doi: 10.1038/srep14423 (2015).